A Multimode Self-Optimization Electrolysis Converting Strategy for Improving Efficiency of Alkaline Water Electrolyzers

Jia Xiong, Yanghong Xia, *Member, IEEE*, Yonggang Peng, *Member, IEEE*, and Wei Wei, *Member, IEEE*

***Abstract*—Alkaline water electrolysis is widely employed for industrial-scale hydrogen production due to its simple structure, low cost, and mature technique. However, the low-load inefficiency of alkaline water electrolyzers (AWEs) results in a narrow operating range (usually 40%–100% of rated power), which makes AWEs hardly follow the fluctuating photovoltaic (PV) power over a wide range. Focusing on this issue, this article proposes a multimode self-optimization electrolysis converting (MMSOEC) strategy and its prototype converter to enhance the efficiency of AWEs. Through the proper combination of dc power and pulse power, the proposed MMSOEC technique can reshape the excitation electric field of AWEs; in this way, the performance of AWEs is greatly enhanced. The effectiveness of the proposed technique is verified through a commercial AWE directly driven by PV arrays. Experimental results show that the efficiency enhancement can be up to 15.4% under the low-load condition as compared to the conventional pure dc power supply.**

***Index Terms*—Alkaline water electrolyzers (AWEs), efficiency enhancement, hydrogen production, multimode self-optimization (MMSO).**

I. Introduction

HYDROGEN has been considered a premium energy carrier due to its zero-carbon emissions, high energy content, and long-term storage. Currently, there are several methods for hydrogen production, including water electrolysis, biological, photolysis, and fossil fuel reforming [1]. Water electrolysis is a particularly promising technology because it facilitates the utilization of renewable energy sources (RESs) to generate pollution-free hydrogen gas, such as solar, wind, and tide energy [2]. Within the field of water electrolysis, alkaline water electrolyzers (AWEs) have aroused considerable interest due to their longer life span, more mature technology, and lower cost compared to proton exchange membrane electrolyzers and solid oxide electrolyzers [3].

Manuscript received 18 July 2023; revised 27 September 2023 and 25 November 2023; accepted 21 December 2023. Date of publication 25 December 2023; date of current version 26 January 2024. This work was supported in part by the Key R&D Program of Zhejiang Province under Grant 2022C01161, in part by the National Natural Science Foundation of China under Grant 52007162, and in part by the Fundamental Research Funds for the Central Universities under Grant 226-2022-00044. Recommended for publication by Associate Editor A. Barrado. *(Corresponding author: Yanghong Xia.)*

The authors are with the College of Electrical Engineering School, Zhejiang University, Hangzhou 310027, China (e-mail: 22110101@zju.edu.cn; royxiayh@zju.edu.cn; pengyg@zju.edu.cn; wwei@zju.edu.cn).

Color versions of one or more figures in this article are available at https://doi.org/10.1109/TPEL.2023.3346897.

Digital Object Identifier 10.1109/TPEL.2023.3346897

Presently, the inefficiency within commercial AWEs has hindered hydrogen from becoming a financially viable energy source in comparison to fossil fuels [4], [5]. It is reported that the majority of energy losses within AWEs are attributed to the overvoltage resulting from the increased electrical impedance between the electrodes [5]. Varying operational parameters, such as electrolysis temperature, electrolyte concentration, and distance between electrodes, can lead to different degrees of improvement in electrolysis efficiency [6], [7], [8]. Nagai et al. [7], [8] established a two-phase flow physical model with the objective of determining the optimal distance between electrodes to minimize the void fraction in the electrolyte resulting from bubbles. To better address this issue, studies have utilized external physical fields to enhance the separation of gas bubbles from the electrodes, such as an ultrasonic field [9], a gravity field [10], and a magnetic field [11]. More recently, a novel capillary-fed electrolysis cell has been proposed to provide bubble-free electrolysis operation for the electrodes, wherein the generated gases readily pass across the porous hydrophobic membrane and the thin layer of electrolytes, rather than forming gas bubbles [12], [13], [14]. However, implementing external physical fields or capillary-fed electrolysis cells presents challenges in terms of system cost and design.

The application of converters is enhanced by the integration of the AWEs and RESs since the voltage provided by the RESs is much higher than the voltage required by the AWEs. As a core device for hydrogen production by water electrolysis, converters generate high-frequency current harmonics that result in additional power dissipation during the electrolysis process [15]. Rectifier topologies have a significant effect on current quality, as demonstrated in [16], where the results show that the pulsewidth modulation (PWM) rectifier composed of semiconductors using forced commutation consumes up to 12% lower electrolyzer stack specific energy than the 12-pulse thyristor rectifier. An interleaved topology, proposed in [17], generates pure dc current by superimposing ripple currents with the same amplitude but complementary phases. Meng et al. [18], [19] were interested in the high power and efficient electrolytic hydrogen production using a novel hybrid rectifier comprising a PWM rectifier and a silicon-controlled rectifier.

The pulse power supply generates a variety of periodic pulses, such as square pulse waves, triangular pulse waves, and trapezoidal pulse waves. These pulses are widely used in various applications, including wastewater treatment [20], biology [21],

and radar transmitters [22]. According to the frequency characteristic of the pulse waveform, the pulse power supply can be classified into the high-frequency pulse and the low-frequency pulse. Results from [23] showed that using high-frequency pulsed electric fields can enhance the mass transfer of gas bubbles, which in turn increases the active electrocatalytic area on the electrodes and reduces the ohmic resistance between the electrodes. However, Vincent et al. [24] and Shimizu et al. [25] attributed the efficiency improvement to the suppression of the electrical double-layer (EDL) formation by the high-frequency pulsed electric field, thereby avoiding the losses from diffusion limitations in the EDL charging and discharging processes. Indeed, from an energy perspective, the high-frequency components in current and voltage have a negative impact on hydrogen production [16], [26]. Regarding high-frequency pulse electrolysis for hydrogen production, in addition to the inconsistent mechanisms analysis and contradictory viewpoints, there are still other issues that need to be addressed. The efficiency comparison between the high-frequency pulse electrolysis and the pure dc electrolysis in [23], [24], and [25] was only made on a lab-scale test electrolyzer, and further experimental verification should be required on industrial-scale AWEs. When the high-frequency pulse is applied to the commercial AWEs, the power converter must simultaneously meet the demanding requirements of the high power and ultrahigh frequency, which presents challenging tasks for power converter design.

In contrast to previous studies, this article aims to improve the low-load efficiency of commercial AWEs by providing innovative insights into the physical structure and electrical characteristics of commercial AWEs. The main contributions of this article can be summarized as follows. First, by utilizing the low-frequency power pulse to reconstruct the internal electric field of the AWEs, the low-load electrolysis efficiency is improved without the need for external physical fields. Second, to validate the applicability of this method in industrial applications, a multimode self-optimization (MMSO) technique and the corresponding prototype converter are proposed. Third, the key parameters in the MMSO electrolysis converting (MMSOEC) strategy are analyzed.

The remainder of this article is organized as follows. In Section II, the physical structure and electrical characteristics of the commercial AWEs are presented, and the mechanism of low-load inefficiency is revealed. Then, in Section III, the MMSO technique combining the low-frequency pulse electrolysis and dc electrolysis is proposed. In Section IV, the converter topology for the AWEs directly driven by PV arrays and the corresponding MMSOEC strategy are introduced in detail and the key parameters of the MMSOEC strategy are analyzed. Experimental results are analyzed in Section V. Finally, Section VI concludes this article.

II. Mechanism of Low-Load Inefficiency

Fig. 1 shows the 3-D structure of the AWEs. The AWEs consist of many electrolysis cells connected in series which are composed of an aqueous solution of potassium hydroxide at 30 wt%, diaphragms, and bipolar electrodes. Traditionally, the

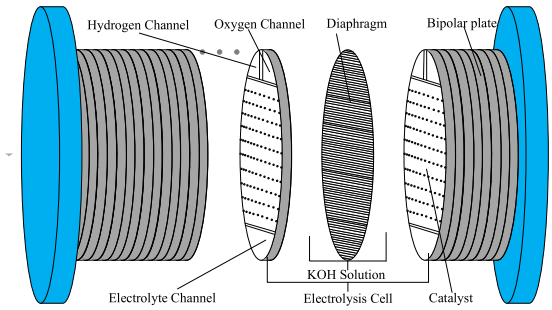

Fig. 1. 3-D structure of the AWEs.

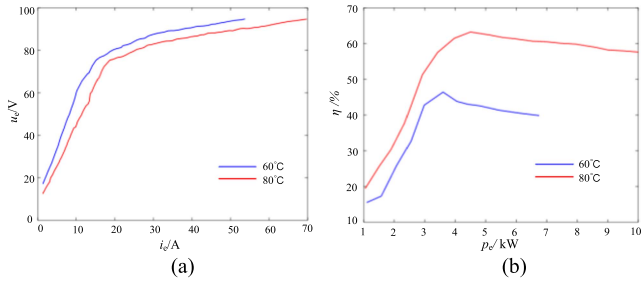

Fig. 2. Experimental static curves for the commercial AWE. (a) *I–U* curves. (b) Electrolysis efficiency versus electrolysis power.

structure of the bipolar electrode can provide shorter current paths and lower resistance of the electrodes compared with the monopolar electrode design [27]. The electrolyte is fed into the AWEs through the electrolyte channel at the bottom, and it is shared by all electrolysis cells.

Oxygen and hydrogen leave the electrolysis cells through the oxygen and hydrogen channels at the top, respectively.

The overall reaction of water electrolysis occurring on the electrodes is expressed as

$$\mathrm{H_2O} + \text{electricity} \rightarrow \mathrm{H_2} + 1/2\mathrm{O_2}. \tag{1}$$

Considering the thermodynamic and electrochemical in the process of electrolysis, assuming that all electrolysis cells have the same energy conversion process, the typical mathematical model obtained from a single electrolysis cell is simply extended to the AWEs [28], [29]

$$u_e = N_e \left(U_{\text{rev}} + \frac{r\,(T)}{A} i_e + s\,(T) \log \left(\frac{t\,(T)}{A} i_e + 1 \right) \right) \tag{2}$$

where u_e is the terminal voltage of the AWEs, i_e is the electrolysis current, N_e is the number of electrolysis cells, U_{rev} is the reversible cell voltage, A is the effective surface area of the electrode, and $r(T)$, $s(T)$, and $t(T)$ are the temperature-dependent overvoltage coefficients.

Fig. 2(a) shows the electrolysis current versus the terminal voltage of the commercial AWE at different temperatures. From the figure, the *I–U* curves can be approximately described as curves consisting of two segments of straight lines with different slopes. The differences between the typical mathematical model and the aforementioned curves are manifested in that the former believes the electrolytic reactions occur and the electrolysis

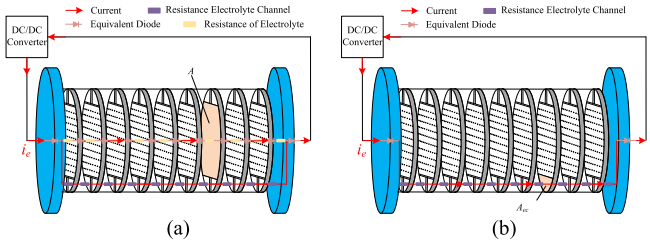

Fig. 3. Current paths under the different operating conditions, where A_{ec} is the area of the electrolyte channel. (a) High-load condition. (b) Low-load condition.

current is not equal to zero only when u_e is greater than $N_e U_{rev}$, whereas the latter shows that current can be generated even when u_e is less than $N_e U_{rev}$.

As shown in Fig. 2(b), during the low-load condition, with the increase of the electrolysis power, the electrolysis efficiency increases slowly. However, the high-load electrolysis efficiency remains relatively stable. Therefore, there exists a unique optimal power corresponding to the maximum efficiency at a specific temperature, namely the maximum-efficiency power P_{op}. The electrolysis efficiency is defined as

$$\eta = \frac{\text{HHV} \int_0^{\Delta t} V_H dt}{\int_0^{\Delta t} u_e i_e dt} \tag{3}$$

where HHV is the high heat value of hydrogen, V_H is the hydrogen flow rate measured, and Δt is the time interval for measuring the hydrogen gas volume.

Fig. 3(a) shows the current path under the high-load condition. From the theory of electrochemistry, it can be inferred that with a sufficiently high terminal voltage, the energy barrier of electrolytic reactions can be overcome, allowing electrons to transfer at the interface between the electrodes and the electrolyte. It means that the AWE can produce electrolytic reactions completely. As shown in Fig. 3(a), it can be seen that the effective surface area of the electrode is greatly larger than the area of the electrolyte channel A_{ec}, resulting in the predominant flow of electrolysis current through the electrodes and electrolyte. The terminal voltage of the electrolysis cell is mainly shared by U_{rev} under the high-load condition, which is equivalent to the forward voltage of a diode as shown in Fig. 3(a), thereby the energy from the external power source is primarily used for electrolytic reactions and producing hydrogen. Additionally, the experimental *I–U* curves for the AWE are in close agreement with the typical mathematical model under the high-load condition, due to the uniform distribution of the excitation electric field.

Compared with the high-load condition, the terminal voltage of the AWE under the low-load condition is insufficient to overcome the energy barrier of electrolytic reactions in all cells. As shown in Fig. 3(b), the current primarily flows through the electrodes at both ends and the electrolyte channel, and only those electrodes at both ends generate electrolytic reactions. The resistance of the electrolyte channel absorbs the majority of the energy from the external power source. Note that even when u_e is greater than $N_e U_{rev}$, the AWE cannot produce electrolytic

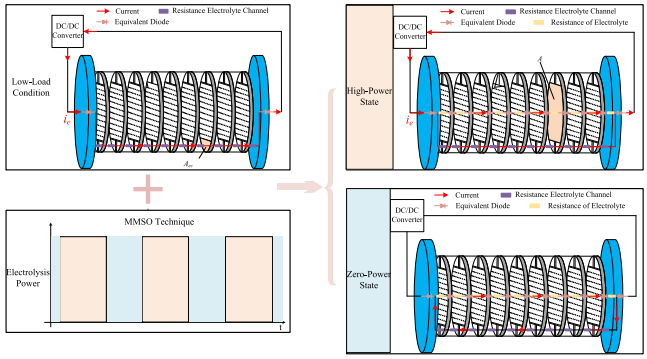

Fig. 4. Electrolysis states based on the MMSO technique under the low-load condition.

reactions completely because the voltage is partially shared by the resistance of the electrolyte. Meanwhile, the electric field distribution in the AWEs is nonuniform, rendering it impossible to fully generalize the *I–U* characteristics of the AWE using the typical mathematical model. Also, the resistance in the low-load condition dominated by the electrolyte channel is greatly larger than the resistance in the high-load condition dominated by the electrolyte between the electrodes, which represents the root cause of the "inefficiency" phenomenon under the low-load condition.

III. Principle of MMSO Technique for AWEs

The analysis of low-load inefficiency reveals that modifying the distribution of the excitation electric field through the power supply can ensure complete electrolytic reactions. The proposed MMSO technique for AWEs consists of two modes. Conventional dc power electrolysis for the high-load condition can keep the economy and efficiency of this system. The electrolysis mode under the low-load condition is switched to the low-frequency pulse power electrolysis to reconstruct the excitation electric field.

The proposed MMSO technique, as depicted in Fig. 4, allows the AWE to operate intermittently at the maximum-efficiency power under the low-load condition. Meanwhile, the excitation electric field under the low-load condition similar to that under the high-load condition can be established. Therefore, the low-load efficiency can behave as well as in the high-load condition. Specifically, the pulse electrolysis within one pulse cycle consists of two major branches, including the zero-power state and the high-power state. The electrolysis power variation is implemented in the following equation by varying the pulse power duty ratio D_e:

$$p_e = \frac{1}{T_{cuk}} \int_0^{T_{ON}} P_{op} dt = D_e P_{op} \tag{4}$$

where T_{cuk} is the low-frequency pulse cycle and T_{ON} is the duration of the high-power state.

The rate at which the excitation electric field is established is associated, mainly, with the EDL effects [29]. With this argument in mind, to accurately model the static–dynamic behavior

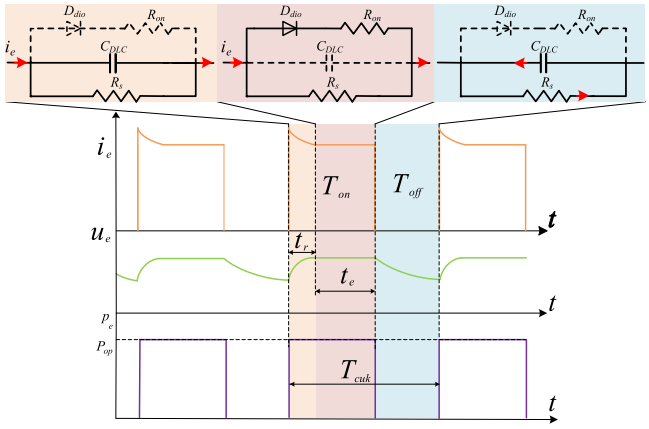

Fig. 5. Dynamic performance of the AWEs under the pulse power electrolysis mode.

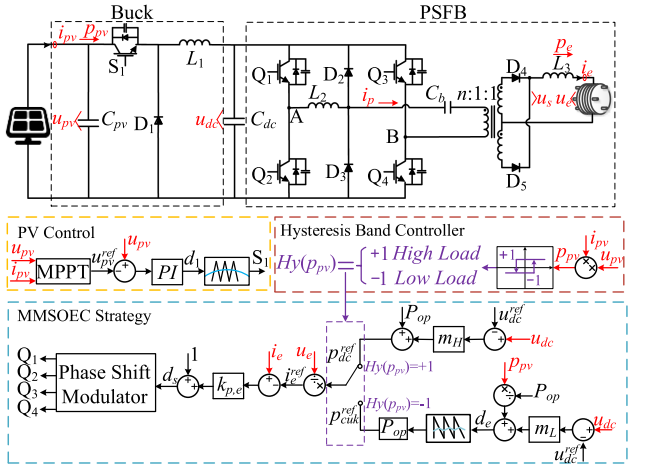

Fig. 6. Overall circuit and controller architecture of the two-stage DC–DC converter.

of the AWEs, the contributions of the overvoltage phenomena and EDL effects have to be taken into consideration. The static–dynamic model of the AWEs is shown in Fig. 5. In this model, the double-layer capacitor C_{DLC} is related to the EDL effects. The thermodynamic phenomena in electrolysis reactions can be modeled by an ideal diode D_{dio} with a forward voltage $N_e U_{\text{rev}}$. R_{ON} and R_s are the impedance of the electrolyte between electrodes and the electrolyte channel, respectively.

Fig. 5 shows the dynamic response of the AWEs under the pulse power electrolysis mode. The dynamic response process can be divided into the following three parts.

1) Voltage rise stage t_r. Considering the power control, i_e increases rapidly to peak current and charges C_{DLC}, and the voltage across D_{dio} continues to increase nonlinearly.
2) Electrolysis stage t_e. The ideal diode D_{dio} conducts when its voltage is above $N_e U_{\text{rev}}$. In the meanwhile, the electrolysis current at the steady state flows through D_{dio} and R_{ON}, mainly. As a consequence, electrolytic reactions can occur completely.
3) Voltage fall stage T_{OFF}. Without power supplied, C_{DLC} is discharging, and its voltage continuously decays, which results in weakening the excitation electric field and turning OFF D_{dio}.

Thus, the power supplied enhances the excitation electric field during t_r aiming at compensating the undesired effects at the voltage fall stage. It can be inferred that electrolysis efficiency increases as the value of t_e/T_{cuk} increases accordingly; since the time used for the electrolytic reactions is increased. In the special case, the larger T_{cuk} contributes to improving the efficiency of the AWEs with fixed dynamic response time, namely t_r and T_{OFF} are constant, but entailing an increase in dc-link capacitor mentioned in (22), shown in Section IV-C. Thus, there is a tradeoff between the electrolysis efficiency and the capacitor.

IV. Two-Stage DC–DC Converter and Control

To achieve the MMSO technique, the two-stage dc–dc converter serving as the interface between the power source and the AWE needs to meet the following requirements.

1) The input current of the two-stage dc–dc converter is constant so that the low-frequency pulse power does not transfer to the input power source, which is beneficial for the high energy conversion efficiency of the PV arrays.
2) A storage capacitor needs to be connected to the dc-link to eliminate instantaneous power difference since the input power of the two-stage dc–dc converter is flat.
3) The back-end converter needs to adjust the operating modes of the AWE based on the PV power. Meanwhile, the AWE needs it to provide a stable power pulse.

A. Converter Topology for AWEs Directly Driven by PV Arrays

Fig. 6 shows the overall circuit architecture of the proposed two-stage dc–dc converter. For the PV arrays with high terminal voltage u_{pv}, a typical buck converter is used. The dc link, where both of the stage converters are connected in series, has a capacitor C_{dc} with a voltage u_{dc}. The phase-shift full bridge (PSFB) with a wide voltage gain is selected as the back-end converter, which is widely employed in dc-high-power applications [30], [31], [32]. The circuit diagram of the PSFB converter, as shown in Fig. 6, consists of the following parts: full bridge circuit, resonant inductor L_2, clamping diodes, namely D_2 and D_3, blocking capacitor C_b, step-down high-frequency-isolation transformer with a turn ratio of $n:1:1$, center-tapped rectifier, and filter inductor L_3. The existence of the double-layer capacitor C_{DLC} eliminates the need for the output capacitor. As shown in Fig. 7(a), the insulated gate bipolar transistors (IGBTs) in the same leg of the full bridge circuit, such as Q_1 and Q_2, have a fixed duty ratio, and complementary switching states. The phase shift duty ratio d_s causes overlapping between the drive signals of the diagonal switch pairs such as Q_1/Q_4 and Q_2/Q_3, which determines the value of the effective duty ratio D_{eff} and the amount of energy transferred from the primary side of the transformer to the secondary side of the transformer. The effective duty ratio of the PSFB converter is given as

$$D_{\text{eff}} = \frac{n(u_e + U_F)}{u_{\text{dc}}} \tag{5}$$

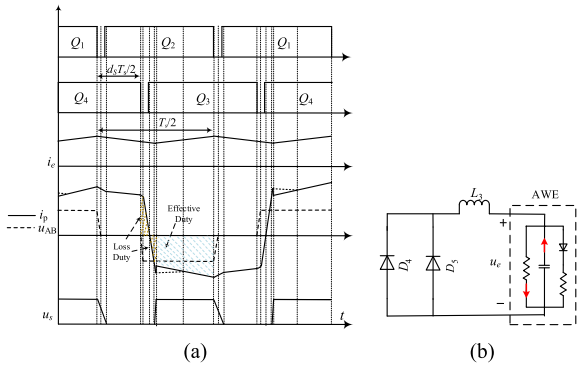

Fig. 7. Key operation states of the PSFB converter. (a) Conventional operating waveforms during the DC power electrolysis, voltage rise stage, and electrolysis stage in pulse power electrolysis, where i_p is the primary current of the transformer, u_{AB} is the output voltage of the full bridge circuit, and u_s is the rectifier voltage. (b) Operational state of the center-tapped rectifier in the PSFB converter during the voltage fall stage.

where U_F is the forward voltage of the rectifier diodes. Due to the effects of duty loss and dead time, the effective duty is less than $(1 - d_s)$.

In pulse power electrolysis mode, the operation mode of the center-tapped rectifier is different from that mentioned in [32]. During the voltage fall stage, the primary current of the transformer gradually decays to zero, and the voltage of the secondary side of the transformer equals zero. The operational state of the center-tapped rectifier in the PSFB converter is shown in Fig. 7(b). A center-tapped rectifier based on reverse-blocking diodes can prevent the current surge of the double-layer capacitor from flowing back into the PV arrays. Thus, there is no need for an additional protection diode required for a nonisolated dc–dc converter [33].

B. Proposed MMSOEC Strategy

The converter topology for AWEs directly driven by PV arrays is presented in Section IV-A. This section will introduce the MMSOEC strategy to meet the requirements of the two-stage dc–dc converter serving as the interface between the power source and the AWE.

The transition point between the pulse power and the dc power is determined by P_{op}. As shown in Fig. 6, when the PV power increases more than P_{op}, the electrolysis mode is changed from pulse power mode to dc power mode. Therefore, the PV power is measured to determine the operation mode. Considering the ultra-short-term fluctuations in PV power, a hysteresis band controller is added to prevent bouncing between these two modes

$$\text{Hy}\left(p_{\text{pv}}\right) = \begin{cases} +1\left(\text{ High Load}\right),\ p_{\text{pv}} > P_{\text{op}},\ \text{Forward} \\ -1\left(\text{ Low Load}\right),\ p_{\text{pv}} < P_{\text{op}} - \Delta P,\ \text{Backward} \end{cases} \tag{6}$$

where p_{pv} is the PV power and ΔP is the hysteresis bandwidth.

The overall controller architecture is depicted in Fig. 6. The dc-link capacitor can realize the power decoupling between the buck and the PSFB converter. Neglecting the loss in the two-stage dc–dc converter, the dynamic equation of the dc-link capacitor voltage can be expressed as

$$C_{\text{dc}} u_{\text{dc}} \frac{du_{\text{dc}}}{dt} = p_{\text{pv}} - p_e. \tag{7}$$

At the same time, the controller of each stage dc–dc converter can be designed, respectively. Maximum power point tracking (MPPT) for the PV arrays can be implemented in the buck converter. The PSFB converter regulates the dc-link voltage, it is responsible for energy balance in this system.

For PV control, as shown in Fig. 6, the MPPT is implemented by adopting the perturbation and observation method, generating a reference voltage $u_{\text{pv}}^{\text{ref}}$, where tracking $u_{\text{pv}}^{\text{ref}}$ using a PI controller with a proportional gain $k_{p,\text{pv}}$ and an integral gain $k_{i,\text{pv}}$ that adjusts the duty ratio of the switch S_1. The control law can be expressed as

$$d_1 = -\left(k_{p,\text{pv}} + \frac{k_{i,\text{pv}}}{s}\right)\left(u_{\text{pv}}^{\text{ref}} - u_{\text{pv}}\right). \tag{8}$$

The control structure of the PSFB is shown in Fig. 6. According to the control function, it can be divided into a dc-link voltage control loop and a current control loop. The dc-link voltage control loop is realized using the droop control and the pulse power duty ratio, both of which are performed by measuring the dc-link voltage.

In the dc power mode, the droop controller is responsible for energy balance, which works as an adaptive function. Its dc-link voltage feedback and output power reference change according to the PV power. The dc power reference for the AWEs is

$$p_{\text{dc}}^{\text{ref}} = -m_H\left(u_{\text{dc}}^{\text{ref}} - u_{\text{dc}}\right) + P_{\text{op}} \tag{9}$$

where m_H is the droop coefficient and $u_{\text{dc}}^{\text{ref}}$ is the rated dc-link voltage.

Second, the pulse power duty ratio is online tuned to adapt to the fluctuating power of PV. The pulse power mode generates the modulating waveform that comprises the dynamic and static parts, which can be expressed as

$$d_e = -m_L\left(u_{\text{dc}}^{\text{ref}} - u_{\text{dc}}\right) + \frac{p_{\text{pv}}}{P_{\text{op}}} \tag{10}$$

where m_L is the proportional coefficient. The static part provides a static operating point, and the dynamic part contributes to maintaining energy balance.

The modulating waveform d_e is compared with the carrier waveform S_c with an amplitude of 1 and a cycle of T_{cuk}, and then multiplying the modulated signal by P_{op} yields the pulse power reference

$$p_{\text{cuk}}^{\text{ref}} = \begin{cases} P_{\text{op}},\ d_e \geq S_c \\ 0,\ d_e < S_c \end{cases}. \tag{11}$$

The inner current loop can enhance the dynamic response of the PSFB converter to rapidly track the pulsed power. A proportional controller modifies the amount of the phase shift duty ratio d_s in accordance with the error between the electrolysis current reference and the measured electrolysis current. Note that using a proportional controller with a high gain can avoid the unstable loop caused by integral corrective action, at the same time, only introducing a little static current error [34]. The control law can

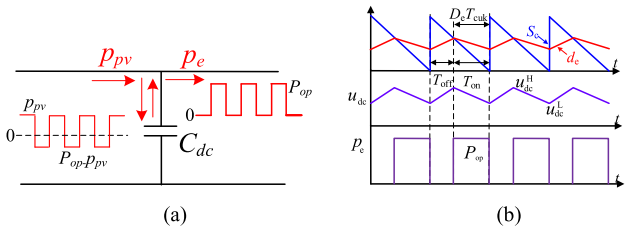

Fig. 8. Pulse power electrolysis. (a) Power balance. (b) Closed-loop dynamics.

be expressed as

$$d_s = 1 - k_{p,e}\left(i_e^{\text{ref}} - i_e\right) \tag{12}$$

where $k_{p,e}$ is the proportional coefficient, and i_e^{ref} is the electrolysis current reference, which can be carried out by the following equation:

$$i_e^{\text{ref}} = \begin{cases} \frac{p_{\text{dc}}^{\text{ref}}}{u_e} & (\text{High Load}) \\ \frac{p_{\text{cuk}}^{\text{ref}}}{u_e} & (\text{Low Load}) \end{cases}. \tag{13}$$

C. Key Parameters Analysis

As shown in Fig. 8(a), when the PV power is below the critical value P_{op}, a storage capacitor is required to eliminate instantaneous power differences. In the proposed topology, the dc-link capacitor C_{dc}, also known as a passive capacitor, is selected as the buffer element to provide the inertial-support power and smooth the pulse power in the two-stage dc–dc converter. Therefore, the remaining part of this section will analyze the value of C_{dc} and the key parameters that are affected by C_{dc}.

Fig. 8(b) shows the overall closed-loop dynamics during the pulse power electrolysis. During this time interval $[0, T_{\text{OFF}}]$, C_{dc} absorbs the PV power, whereas the operating power of the AWE is zero. During this time interval $[T_{\text{OFF}}, T_{\text{cuk}}]$, it also needs to feed additional power, namely $(P_{\text{op}} - p_{\text{pv}})$, required by the AWE. The dc-link voltage versus the PV power and electrolysis power is given by the following equation:

$$\begin{cases} \frac{1}{2}C_{\text{dc}}u_{\text{dc}}^2 - \frac{1}{2}C_{\text{dc}}\left(u_{\text{dc}}^L\right)^2 = p_{\text{pv}} \cdot t \; t \in [0, T_{\text{OFF}}] \\ \frac{1}{2}C_{\text{dc}}\left(u_{\text{dc}}^H\right)^2 - \frac{1}{2}C_{\text{dc}}\,u_{\text{dc}}^2 = (P_{\text{op}} - p_{\text{pv}}) \\ \quad \cdot (t - T_{\text{OFF}}) \; t \in [T_{\text{OFF}}, T_{\text{cuk}}] \end{cases} \tag{14}$$

where u_{dc}^H and u_{dc}^L represent the peak and valley values of the dc-link voltage, respectively.

In the aforementioned time intervals, the variation of the energy stored in the capacitor can be expressed as follows:

$$\begin{cases} \frac{1}{2}C_{\text{dc}}\left(u_{\text{dc}}^H\right)^2 - \frac{1}{2}C_{\text{dc}}\left(u_{\text{dc}}^L\right)^2 = p_{\text{pv}} \cdot T_{\text{OFF}} \\ \frac{1}{2}C_{\text{dc}}\left(u_{\text{dc}}^H\right)^2 - \frac{1}{2}C_{\text{dc}}\left(u_{\text{dc}}^L\right)^2 = (P_{\text{op}} - p_{\text{pv}}) \cdot T_{\text{ON}} \end{cases}. \tag{15}$$

An expression for the pulse power duty ratio D_e can be obtained as follows from (4) and (15):

$$D_e = \frac{T_{\text{ON}}}{T_{\text{cuk}}} = \frac{p_{\text{pv}}}{P_{\text{op}}}. \tag{16}$$

Moreover, u_{dc} during this time interval $[T_{\text{OFF}}, T_{\text{cuk}}]$ can be calculated from (14) and (16) as

$$u_{\text{dc}} = \sqrt{\left(u_{\text{dc}}^H\right)^2 - \frac{2P_{\text{op}}\left(1 - D_e\right)\left(t - T_{\text{OFF}}\right)}{C_{\text{dc}}}}. \tag{17}$$

Combining (10), (16), and (17), the modulating waveform can be rewritten as

$$d_e\left(t\right) = -m_L\left(u_{\text{dc}}^{\text{ref}} - \sqrt{\left(u_{\text{dc}}^H\right)^2 - \frac{2P_{\text{op}}\left(1-D_e\right)\left(t-T_{\text{OFF}}\right)}{C_{\text{dc}}}}\right) + \frac{p_{\text{pv}}}{P_{\text{op}}}. \tag{18}$$

From Fig. 8(b), $d_e(t)$ equals $S_{\text{C}}\left(t\right) = 1 - \frac{t}{T_{\text{cuk}}}$ when $t = T_{\text{OFF}}$, such that

$$u_{\text{dc}}^{\text{ref}} = u_{\text{dc}}^H. \tag{19}$$

In practice, u_{dc}^H is less than $u_{\text{dc}}^{\text{ref}}$ since the loss of the two-stage dc–dc converter and the equivalent series resistance of the dc-link capacitor are not taken into consideration.

Submitting (19) into (15), then u_{dc}^{L} can be calculated as

$$u_{\text{dc}}^L = \sqrt{\left(u_{\text{dc}}^{\text{ref}}\right)^2 - \frac{2P_{\text{op}}\left(1 - D_e\right)D_eT_{\text{cuk}}}{C_{\text{dc}}}}. \tag{20}$$

Typically, P_{op}, T_{cuk}, and C_{dc} are constant, and thus, combined with (20), u_{dc}^L reaches a minimum value $u_{\text{dc}}^{\min}$ when D_e equals 0.5

$$u_{\text{dc}}^{\min} = \sqrt{\left(u_{\text{dc}}^{\text{ref}}\right)^2 - \frac{P_{\text{op}}T_{\text{cuk}}}{2C_{\text{dc}}}}. \tag{21}$$

Equation (21) shows that a smaller $u_{\text{dc}}^{\min}$ is beneficial for reducing the capacitance of the dc-link capacitor. As shown in Fig. 9, when u_{dc} falls to its minimum value $u_{\text{dc}}^{\min}$, the effective duty margin, namely $(1 - D_{\text{eff}})$, reaches its lowest value. As the effective duty margin decreases, it results in slow dynamic and reduced load capacity of the converter [35], [36]. Thus, when a smaller capacitor is selected, the effective duty margin should be taken into consideration. Considering the dead time of high-power IGBTs and duty loss, a maximum effective duty ratio of 0.75 is chosen. According to Fig. 2(a), it can be inferred that when the maximum-efficiency power is approximately 4.5 kW, the terminal voltage of the AWEs is around 92 V. By substituting $D_{\text{eff}} = 0.75$, $u_{\text{e}} = 92\,\text{V}$, $U_{\text{F}} = 1.75\,\text{V}$, and $n = 3.2$ into (5), the value of $u_{\text{dc}}^{\min}$ is obtained to be 400 V.

To limit u_{dc} to the allowable voltage $[u_{\text{dc}}^{\min}, u_{\text{dc}}^{\text{ref}}]$, and the dc-link capacitance is designed by the formula of

$$C_{\text{dc}} \geq \frac{P_{\text{op}}T_{\text{cuk}}}{2\left[\left(u_{\text{dc}}^{\text{ref}}\right)^2 - \left(u_{\text{dc}}^{\min}\right)^2\right]}. \tag{22}$$

Fig. 10 shows the unstable response of the MMSOEC strategy. When the larger coefficient m_L is used in the MMSOEC strategy, the modulating wave d_e oscillates around the sawtooth-shaped carrier S_c, introducing high-frequency interference into the power reference $P_{\text{cuk}}^{\text{ref}}$. The electrolysis current contains a significant amount of high-order harmonics due to the fast

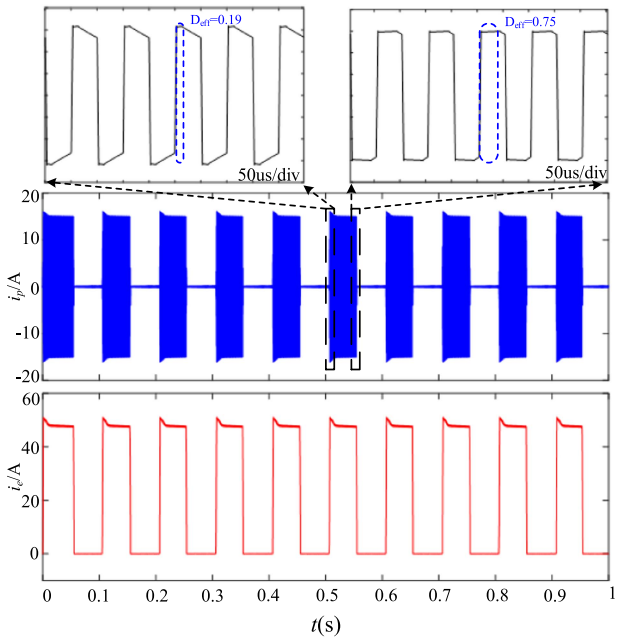

Fig. 9. Steady performance of the PSFB converter.

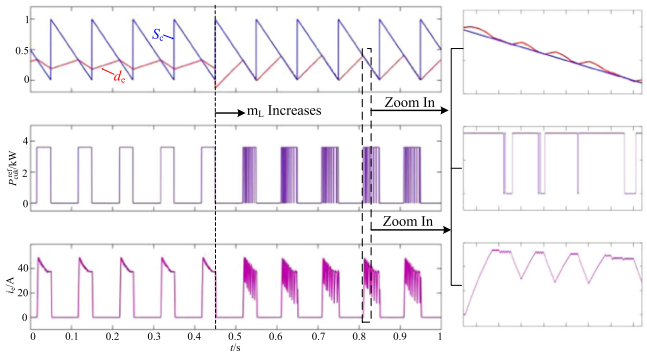

Fig. 10. Stable and unstable responses of the MMSOEC strategy.

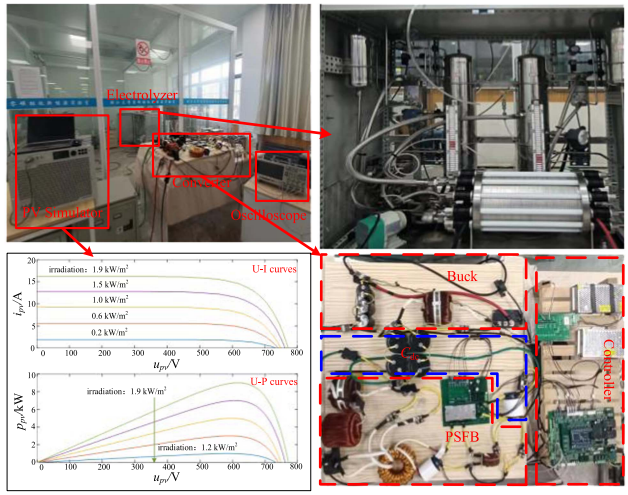

Fig. 11. Experimental platform for hydrogen production by the AWEs directly driven by PV arrays.

TABLE I
SPECIFICATIONS FOR TWO-STAGE DC–DC CONVERTER

Buck Converter		
Items	Symbols	Types/Values
PV Output Capacitor Value	C_{pv}	330 μF
IGBT	S_1	PM200DV1A120
Diode	D_1	DSEP2x61-12A
Inductor Value	L_1	1 mH
DC-link Capacitor Value	C_{dc}	6.9 mF
Phase-shift Full Bridge Converter		
Full Bridge IGBTs	Q_1–Q_4	PM75RL1A120
Resonant Inductor Value	L_2	45 μH
Clamping Diodes	D_2 and D_3	DSEI2x31-12B
Blocking Capacitor Value	C_b	100 μF
Turn Ratio of Transformer	n	3.2
Rectifier Diodes	D_4 and D_5	DSEI2x101-12A
Filter Inductor Value	L_3	2 mH

response of the current control loop [37]. A sufficient condition for system stability is that the slopes of the modulating wave are greater than the slopes of the carrier during the time interval $[T_{\mathrm{OFF}}, T_{\mathrm{cuk}}]$. Therefore, the criteria for system stability is based on the following considerations:

$$\left(\frac{\partial d_e}{\partial t}\right)_{\min} > -\frac{1}{T_{\mathrm{cuk}}}\ t \in [T_{\mathrm{OFF}}, T_{\mathrm{cuk}}]\,. \tag{23}$$

Furthermore, (23) can be further simplified as

$$m_L < \frac{C_{\mathrm{dc}} u_{\mathrm{dc}}^L}{P_{\mathrm{op}}\,(1-D_e)\,T_{\mathrm{cuk}}}. \tag{24}$$

V. EXPERIMENTS

To confirm the validity of the proposed MMSO technique, the experimental platform for hydrogen production by the AWEs directly driven by PV arrays has been established. As shown in Fig. 11, this experimental platform consists of a PV simulator, a commercial AWE, a two-stage dc–dc converter, and a digital processor DSPTMS320F28335. The commercial AWE consists of 48 electrolysis cells connected in series and its rated power is about 10 kW. Each bipolar electrode has an effective electrode area of 133 cm^2. The commercial AWE is equipped with a proton flow meter to measure the hydrogen production rate. The PV simulator is programmed to simulate the PV power fluctuations by time-varying irradiation from 0.2 to 1.9 $\mathrm{kW/m}^2$. As the irradiation increased, the terminal voltage of PV arrays at maximum power point increased from 587 to 615 V. Experimental measurements and control techniques are implemented in the DSPTMS320F28335 with a fixed control cycle of 100 ms. The specifications for the two-stage dc–dc converter are shown in Table I. The dc-link voltage allowable range is [400 V, 500 V], and the switching frequency is 10 kHz. By substituting the corresponding data from Table I into (22), the critical value of the dc-link capacitor is determined to be 6.7 mF. The value of the dc-link capacitor is chosen as 6.9 mF, taking into account the effect of the equivalent series resistance of the electrolytic

TABLE II
CONTROL PARAMETERS OF TWO-STAGE DC–DC CONVERTER

Parameters	Values	Parameters	Values
T_{cuk}	0.1	u_{dc}^{ref}	440
ΔP	500	m_H	100
$k_{p,pv}$	0.001	m_L	0.005
$k_{i,pv}$	0.01	$k_{p,e}$	0.2

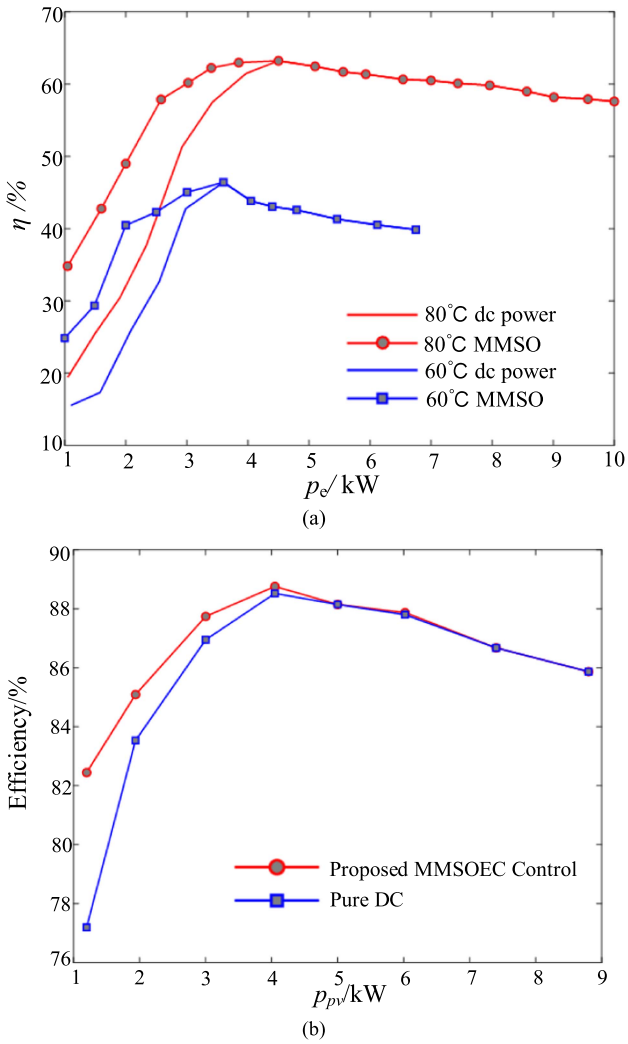

Fig. 12. System efficiency. (a) Electrolysis efficiency. (b) Converter efficiency.

capacitor. The control parameters of the converter are shown in Table II.

A. System Efficiency and System Dynamic Response Results

Fig. 12(a) shows the electrolysis efficiency under different electrolysis modes. The AWE achieves an optimal electrolysis efficiency of approximately 46.4% at a temperature of 60 °C and a pressure of 0.1 MPa, with a corresponding power of 3.6 kW. For the AWE at 80 °C and 0.1 MPa, the optimal electrolysis efficiency is about 63.2%, with an electrolysis power of around 4.5 kW. At 60 °C, the electrolysis efficiency is increased from

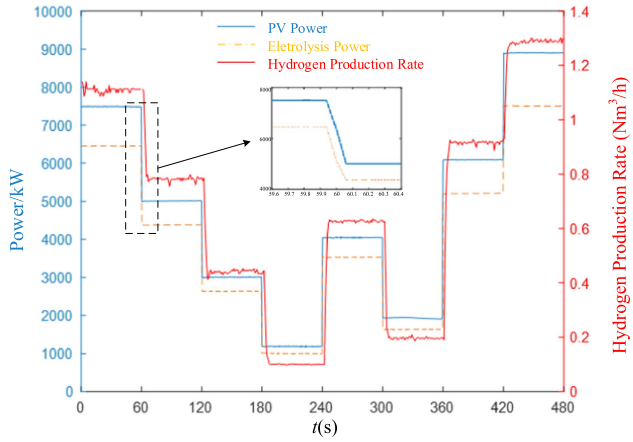

Fig. 13. Overall dynamic performance over the entire load range at 80 °C.

29.4% to 17.3% at 15% of the rated load, and improved efficiency by over 1.7 times. At 80 °C, the electrolysis efficiency increased by 15.4% when the AWE operates at 10% of the rated load. The electrolysis efficiency with pulse power still increases as electrolysis power increases in low load ranges, limited by t_r, as shown in Fig. 13. It should be noted that the efficiency with pulse power at 60 °C is higher than the efficiency with dc power at 80 °C in operation ranges below 25% of the rated load, which indicates pulse power may be a more effective method for improving electrolysis efficiency compared with the increased electrolysis temperature. To compare the converter efficiency in pure dc electrolysis and the MMSO technique, a two-stage dc–dc converter with a fixed dc-link voltage of 420 V is designed for pure dc electrolysis under the low-load condition. Fig. 12(b) shows the converter efficiency, indicating that the proposed MMSOEC control improves converter efficiency by up to 5% compared to pure dc electrolysis. Thus, the proposed MMSOEC control has overall benefits in reducing energy dissipation in the hydrogen production system.

Fig. 13 shows the dynamic performance of PV power, average electrolysis power, and hydrogen production rate over the entire load range at 80 °C, where the average electrolysis power is obtained from a mean value discrete filter with a sampling period of 100 ms and the number of samples of 3000. During the pulse power, the hydrogen production rate is smooth due to the existence of inertial components, such as the pipeline and counterbalance valve. As shown in Fig. 13, the PV arrays achieve maximum power output when the irradiance fluctuates between 0.2 and 1.9 kW/m^2. With the help of the favorable dynamic response of a two-stage dc–dc converter, the PV arrays and AWE are capable of achieving excellent power matching in the transient processes. Throughout the entire process, the rate of hydrogen production is directly proportional to the power used in electrolysis.

B. Transient and Steady Performances of Two-Stage DC–DC Converter Under the MMSOEC Strategy

Fig. 14 shows transient performance with the proposed MMSOEC strategy at 80 °C. Fig. 14(a) shows the results of the

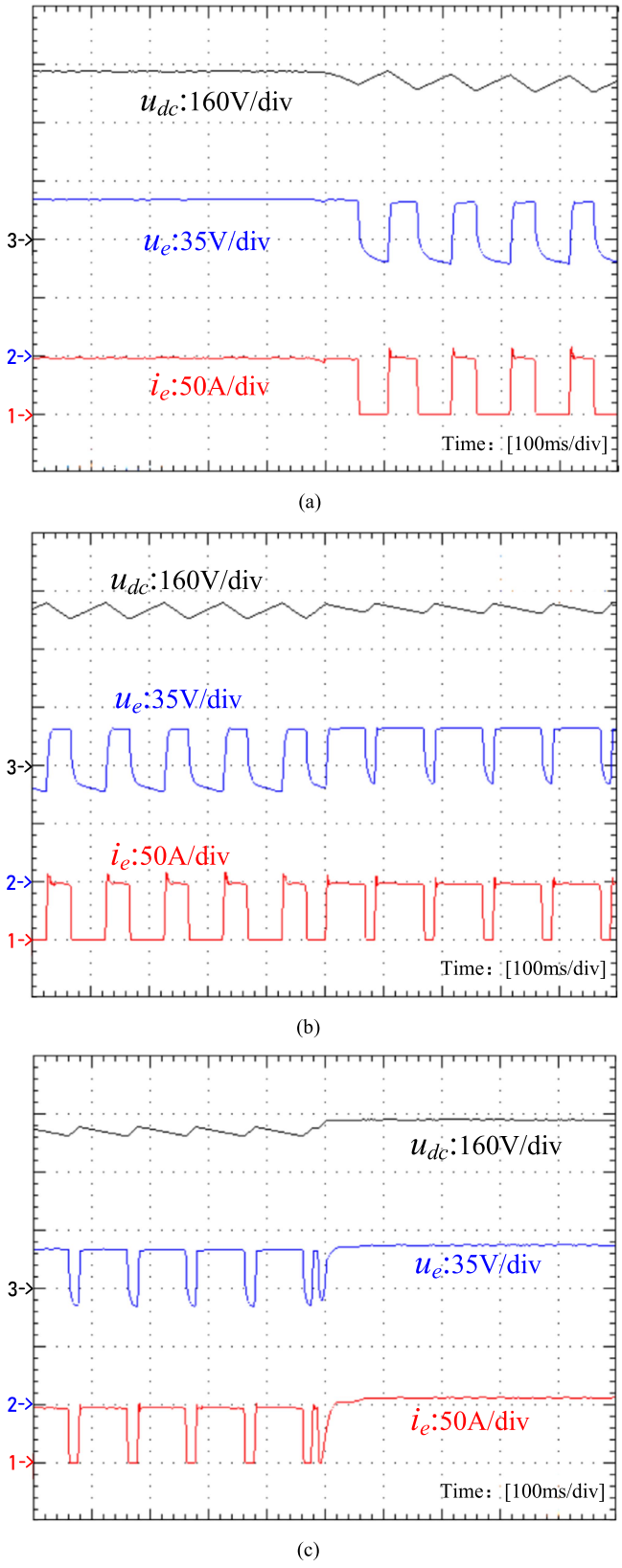

Fig. 14. Transient performance with the MMSOEC strategy at 80 °C. (a) Transient performance, DC power to pulse power, and electrolysis power changes from 5 to 2 kW. (b) Transient performance, pulse power to pulse power, and electrolysis power changes from 2 to 4 kW. (c) Transient performance, pulse power to DC power, and electrolysis power changes from 4 to 6 kW.

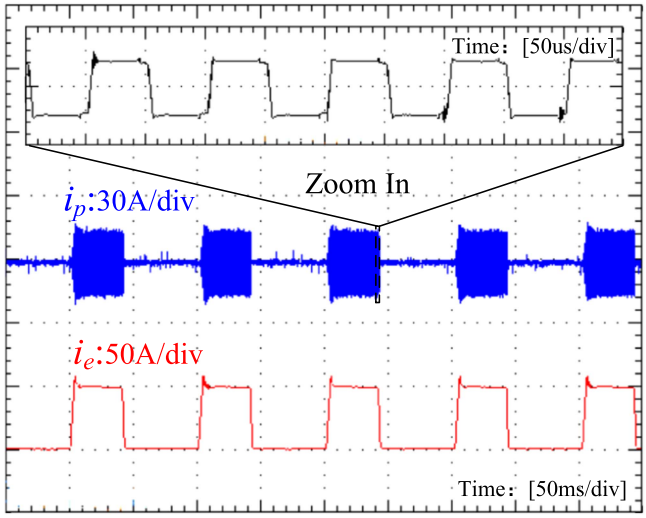

Fig. 15. Steady performance when the electrolysis power is 2 kW.

transition performance from dc power to pulse power. It can be seen that u_{e} and i_{e} gradually decrease and there is no oscillation in u_e, i_e, and u_{dc} due to the existence of a hysteresis band controller, indicating that different electrolysis modes can be switched seamlessly. Fig. 14(b) shows the experimental results of the transition performance from pulse power to pulse power. During the pulse power cycle, with the online-tuned pulse power duty ratio generated by the MMSO technique, the changes of u_{e}, i_{e}, and u_{dc} are synchronous. It can be seen that the pulse power duty ratio is proportional to the electrolysis power, the pulse power duty ratio increases as electrolysis power increases. The dc-link capacitor C_{dc} is used as the buffer element to provide the inertial-support power for the two-stage dc–dc converter, and the dc-link voltage can be kept within the allowable range [400 V, 500 V]. Fig. 14(c) shows experimental results of the transition performance from pulse power to dc power, which is similar to the results in Fig. 14(a).

Fig. 15 shows the steady performance when the electrolysis power is 2 kW. During the zero-power state, the primary current of the transformer i_p gradually decays to zero, and no energy is transferred from the primary side of the transformer to the secondary side. During the high-power state, the primary current of the transformer i_p has a fixed frequency of 10 kHz, and the energy at the primary side of the transformer is transferred to the secondary side for electrolysis reaction. As shown in Figs. 14 and 15, when the dc-link voltage is kept within the range [400 V, 440 V], the converter stall retains a portion of the effective duty margin.

C. *Verification of Key Parameters for System Stability*

Fig. 16 shows the impact of m_L on the stability of the system at 60°, where the PV power is equal to 1 kW and P_{op} is equal to 3.6 kW. The stable critical value of m_L can be obtained through (24) as 0.011. When the value of m_L is changed from 0.005 to 0.015, the system becomes unstable. The high-frequency current

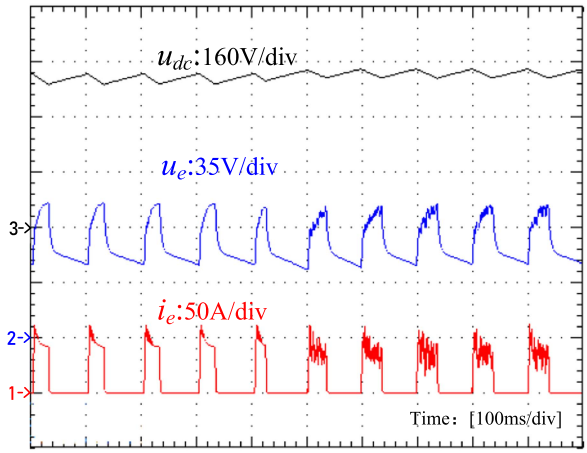

Fig. 16. Impact of m_L on the stability of the system.

harmonics generate additional power losses, which have a detrimental impact on the electrolysis efficiency. The experimental results are highly consistent with the simulation-based results presented in Fig. 10.

VI. Conclusion

In this article, the MMSO technique is investigated to enhance the electrolysis efficiency of the AWEs. The technique focuses on the physical structure and electrical characteristics of commercial AWEs and utilizes the low-frequency pulse to reconstruct the internal electric field of the AWEs. To achieve MPPT for the PV arrays and enable multimode operation of the AWE, the MMSOEC strategy is proposed based on a two-stage dc–dc converter. Additionally, the dc-link capacitor and the key parameters in the pulse electrolysis mode are analyzed in detail. Experimental results show that, with the help of the MMSO technique, the low-load electrolysis efficiency of the commercial AWEs is significantly enhanced. Furthermore, compared to the pure dc electrolysis mode, the converter efficiency is improved in the pulse electrolysis mode. Therefore, the MMSO technique may be a more effective method for improving electrolysis efficiency compared with the increased electrolysis temperature.

References

[1] P. Nikolaidis and A. Poullikkas, "A comparative overview of hydrogen production processes," *Renewable Sustain. Energy Rev.*, vol. 67, pp. 597–611, Jan. 2017.
[2] M. G. Dozein, A. M. De Corato, and P. Mancarella, "Virtual inertia response and frequency control ancillary services from hydrogen electrolyzers," *IEEE Trans. Power Syst.*, vol. 38, no. 3, pp. 2447–2459, May 2023.
[3] W. Pei, X. Zhang, W. Deng, C. Tang, and L. Yao, "Review of operational control strategy for DC microgrids with electric-hydrogen hybrid storage systems," *CSEE J. Power Energy Syst.*, vol. 8, no. 2, pp. 329–346, Mar. 2022.
[4] A. Ursua, L. M. Gandia, and P. Sanchis, "Hydrogen production from water electrolysis: Current status and future trends," *Proc. IEEE*, vol. 100, no. 2, pp. 410–426, Feb. 2012.
[5] N. A. Burton, R. V. Padilla, A. Rose, and H. Habibullah, "Increasing the efficiency of hydrogen production from solar powered water electrolysis," *Renewable Sustain. Energy Rev.*, vol. 135, Jan. 2021, Art. no. 110255.
[6] S. Ding et al., "Analysis of the effect of characteristic parameters and operating conditions on exergy efficiency of alkaline water electrolyzer," *J. Power Sources*, vol. 537, Jul. 2022, Art. no. 231532.
[7] N. Nagai, M. Takeuchi, T. Kimura, and T. Oka, "Existence of optimum space between electrodes on hydrogen production by water electrolysis," *Int. J. Hydrogen Energy*, vol. 28, no. 1, pp. 35–41, Jan. 2003.
[8] N. Nagai, M. Takeuchi, and M. Nakao, "Effects of generated bubbles between electrodes on efficiency of alkaline water electrolysis," *JSME Int. J., Ser. B Fluids Thermal Eng.*, vol. 46, no. 4, pp. 549–556, 2003.
[9] M.-Y. Lin and L.-W. Hourng, "Ultrasonic wave field effects on hydrogen production by water electrolysis," *J. Chin. Inst. Eng.*, vol. 37, no. 8, pp. 1080–1089, Nov. 2014.
[10] M. Wang, Z. Wang, and Z. Guo, "Water electrolysis enhanced by super gravity field for hydrogen production," *Int. J. Hydrogen Energy*, vol. 35, no. 8, pp. 3198–3205, Apr. 2010.
[11] T. Weier, D. Baczyzmalski, J. Massing, S. Landgraf, and C. Cierpka, "The effect of a Lorentz-force-driven rotating flow on the detachment of gas bubbles from the electrode surface," *Int. J. Hydrogen Energy*, vol. 42, no. 33, pp. 20923–20933, Aug. 2017.
[12] A. Hodges et al., "A high-performance capillary-fed electrolysis cell promises more cost-competitive renewable hydrogen," *Nature Commun.*, vol. 13, no. 1, Mar. 2022, Art. no. 1304.
[13] G. Tsekouras et al., "Insights into the phenomenon of 'bubble-free' electrocatalytic oxygen evolution from water," *Sustain. Energy Fuels*, vol. 5, no. 3, pp. 808–819, Feb. 2021.
[14] P. Tiwari, G. Tsekouras, K. Wagner, G. F. Swiegers, and G. G. Wallace, "A new class of bubble-free water electrolyzer that is intrinsically highly efficient," *Int. J. Hydrogen Energy*, vol. 44, no. 42, pp. 23568–23579, Sep. 2019.
[15] V. Ruuskanen et al., "Power quality estimation of water electrolyzers based on current and voltage measurements," *J. Power Sources*, vol. 450, Feb. 2020, Art. no. 227603.
[16] J. Koponen, V. Ruuskanen, A. Kosonen, M. Niemela, and J. Ahola, "Effect of converter topology on the specific energy consumption of alkaline water electrolyzers," *IEEE Trans. Power Electron.*, vol. 34, no. 7, pp. 6171–6182, Jul. 2019.
[17] D. Guilbert, D. Sorbera, and G. Vitale, "A stacked interleaved DC-DC buck converter for proton exchange membrane electrolyzer applications: Design and experimental validation," *Int. J. Hydrogen Energy*, vol. 45, no. 1, pp. 64–79, Jan. 2020.
[18] X. Meng, M. Chen, M. He, X. Wang, and J. Liu, "A novel high power hybrid rectifier with low cost and high grid current quality for improved efficiency of electrolytic hydrogen production," *IEEE Trans. Power Electron.*, vol. 37, no. 4, pp. 3763–3768, Apr. 2022.
[19] X. Meng, L. Jiang, M. He, X. Wang, and J. Liu, "A novel multi-scale frequency regulation method of hybrid rectifier and its specific application in electrolytic hydrogen production," *IEEE Trans. Power Electron.*, vol. 38, no. 1, pp. 123–129, Jan. 2023.
[20] X. Guo, D. Zheng, and F. Blaabjerg, "Power electronic pulse generators for water treatment application: A review," *IEEE Trans. Power Electron.*, vol. 35, no. 10, pp. 10285–10305, Oct. 2020.
[21] W. Zeng et al., "A novel high-frequency bipolar pulsed power generator for biological applications," *IEEE Trans. Power Electron.*, vol. 35, no. 12, pp. 12861–12870, Dec. 2020.
[22] S. Pi, Q. Yu, T. Wang, and J. Lin, "A Marx-based Gaussian monocycle pulse generator with low ringing level for ground penetrating radar applications," *IEEE Trans. Power Electron.*, vol. 38, no. 8, pp. 9907–9916, Aug. 2023.
[23] N. Demir, M. F. Kaya, and M. S. Albawabiji, "Effect of pulse potential on alkaline water electrolysis performance," *Int. J. Hydrogen Energy*, vol. 43, no. 36, pp. 17013–17020, Sep. 2018.
[24] I. Vincent, B. Choi, M. Nakoji, M. Ishizuka, K. Tsutsumi, and A. Tsutsumi, "Pulsed current water splitting electrochemical cycle for hydrogen production," *Int. J. Hydrogen Energy*, vol. 43, no. 22, pp. 10240–10248, May 2018.
[25] N. Shimizu, S. Hotta, T. Sekiya, and O. Oda, "A novel method of hydrogen generation by water electrolysis using an ultra-short-pulse power supply," *J. Appl. Electrochem.*, vol. 36, no. 4, pp. 419–423, Feb. 2006.
[26] Z. Dobó and Á. B. Palotás, "Impact of the voltage fluctuation of the power supply on the efficiency of alkaline water electrolysis," *Int. J. Hydrogen Energy*, vol. 41, no. 28, pp. 11849–11856, Jul. 2016.
[27] O. Ulleberg, "Modeling of advanced alkaline electrolyzers: A system simulation approach," *Int. J. Hydrogen Energy*, vol. 28, no. 1, pp. 21–33, Jan. 2003.

[28] E. Amores, J. Rodríguez, and C. Carreras, "Influence of operation parameters in the modeling of alkaline water electrolyzers for hydrogen production," *Int. J. Hydrogen Energy*, vol. 39, no. 25, pp. 13063–13078, Aug. 2014.
[29] A. Ursua and P. Sanchis, "Static–dynamic modelling of the electrical behaviour of a commercial advanced alkaline water electrolyser," *Int. J. Hydrogen Energy*, vol. 37, no. 24, pp. 18598–18614, Dec. 2012.
[30] Y.-S. Lai, Z.-J. Su, and W.-S. Chen, "New hybrid control technique to improve light load efficiency while meeting the hold-up time requirement for two-stage server power," *IEEE Trans. Power Electron.*, vol. 29, no. 9, pp. 4763–4775, Sep. 2014.
[31] D. S. Gautam and A. K. S. Bhat, "A comparison of soft-switched dc-to-dc converters for electrolyzer application," *IEEE Trans. Power Electron.*, vol. 28, no. 1, pp. 54–63, Jan. 2013.
[32] W. Chen, X. Ruan, and R. Zhang, "A novel zero-voltage-switching PWM full bridge converter," *IEEE Trans. Power Electron.*, vol. 23, no. 2, pp. 793–801, Mar. 2008.
[33] Y. Xia, H. Cheng, H. He, Z. Hu, and W. Wei, "Efficiency enhancement for alkaline water electrolyzers directly driven by fluctuating PV power," *IEEE Trans. Ind. Electron.*, to be published, doi: 10.1109/TIE.2023.3288146.
[34] P. Thounthong, S. Rael, and B. Davat, "Control strategy of fuel cell and supercapacitors association for a distributed generation system," *IEEE Trans. Ind. Electron.*, vol. 54, no. 6, pp. 3225–3233, Dec. 2007.
[35] I.-H. Cho, K.-M. Cho, J.-W. Kim, and G.-W. Moon, "A new phase-shifted full-bridge converter with maximum duty operation for server power system," *IEEE Trans. Power Electron.*, vol. 26, no. 12, pp. 3491–3500, Dec. 2011.
[36] Y.-S. Lai and Z.-J. Su, "Novel on-line maximum duty point tracking technique to improve two-stage server power efficiency and investigation into its impact on hold-up time," *IEEE Trans. Ind. Electron.*, vol. 61, no. 5, pp. 2252–2263, May 2014.
[37] X. Gao, H. Wu, S. Gao, Z. Zhang, and Y. Xing, "A two-stage pulsed power supply for low-DC-voltage and low-frequency pulsed-current loads," *IEEE Trans. Power Electron.*, vol. 36, no. 2, pp. 2298–2309, Feb. 2021.

Jia Xiong received the B.S. degree in electrical engineering from the College of Electrical Engineering, Beijing Jiaotong University, Beijing, China, in 2021. He is currently working toward the M.S. degree in control theory and control engineering with the College of Electrical Engineering, Zhejiang University, Hangzhou, China.

His current research focuses on power electronic converters for electrolytic water hydrogen production in renewable energy systems.

Yanghong Xia (Member, IEEE) received the B.S. degree in automation from the College of Automation, Huazhong University of Science and Technology, Wuhan, China, in 2014, and the Ph.D. degree in control theory and control engineering from the College of Electrical Engineering, Zhejiang University (ZJU), Hangzhou, China, in 2019.

From 2019 to 2020, he was a Postdoctoral Research Fellow with the joint postdoctoral fellowship program between ZJU and the University of Cambridge, Cambridge, U.K. He is currently with the College of Electrical Engineering, ZJU. His research interests include hydrogen production, renewable energy sources, advanced control methods, stability analysis of power systems, and hybrid ac/dc microgrids.

Yonggang Peng (Member, IEEE) received the B.S. degree in automation and the M.S. and Ph.D. degrees in control theory and control engineering from the College of Electrical Engineering, Zhejiang University, Hangzhou, China, in 2001, 2004, and 2008, respectively.

He is currently a Professor with the College of Electrical Engineering, Zhejiang University. His research interests include distributed generation, microgrids, and hybrid ac/dc power systems.

Wei Wei (Member, IEEE) received the B.Eng. degree in automation, the M.Eng. degree in control theory and control engineering, and the D.Eng. degree in power electronics and electronic drives from the College of Electrical Engineering, Zhejiang University, Hangzhou, China, in 1983, 1986, and 1994, respectively.

He is currently a Professor with the College of Electrical Engineering, Zhejiang University. His research interests include intelligent control, the development of novel technology of renewable energy, and smart grids.